Inherent biophysical properties modulate the toxicity of soluble amyloidogenic light chains

Martina Maritan[1], Margherita Romeo[2], Luca Oberti[1], Pietro Sormanni[3], Masayoshi Tasaki[4,8], Rosaria Russo[5], Arianna Ambrosetti[1], Paolo Motta[5], Paola Rognoni[4], Giulia Mazzini[4], Alberto Barbiroli[6], Giovanni Palladini[4], Michele Vendruscolo[3], Luisa Diomede[2], Martino Bolognesi[1,7], Giampaolo Merlini[4], Francesca Lavatelli[4]*, Stefano Ricagno[1]*

[1] Dipartimento di Bioscienze, Università degli Studi di Milano, Via Celoria 26 - 20133 Milano, Italia.

[2] Dipartimento di Biochimica Molecolare e Farmacologia Molecolare, Istituto di Ricerche Farmacologiche Mario Negri IRCCS, 20156, Milano, Italia.

[3] Centre for Misfolding Diseases, Department of Chemistry, University of Cambridge, Cambridge CB2 1EW, United Kingdom.

[4] Amyloidosis Research and Treatment Center, Fondazione IRCCS Policlinico San Matteo, and Dipartimento di Medicine Molecolare, Università di Pavia, Piazzale Golgi 19 - 27100, Pavia, Italia.

[5] Dipartimento di Fisiopatologia Medico-Chirurgica e dei Trapianti, Università degli Studi di Milano, Italia.

[6] Dipartimento di Scienze per gli Alimenti, la Nutrizione e l'Ambiente, Università degli Studi di Milano, 20133, Milano, Italia.

[7] Centro di Ricerca Pediatrica Romeo ed Enrica Invernizzi, Università degli Studi di Milano, Via Celoria 26 - 20133 Milano, Italia.

[8] Department of Morphological and Physiological Sciences, Graduate School of Health Sciences, Kumamoto University, 4-24-1 Kuhonji, and Department of Neurology, Graduate School of Medical Sciences, 1-1-1, Honjo, Kumamoto, Japan.

* to whom correspondence should be addressed:
Stefano Ricagno
Department of Biosciences, University of Milan
Via Celoria 26 20133, Milan Italy
Tel: +390250314914
Email: Stefano.ricagno@unimi.it

Francesca Lavatelli
Department of Molecular Medicine, University of Pavia,
Piazzale Golgi 19 - 27100, Pavia, Italia
Tel: +390382502984
Email: Francesca.Lavatelli@unipv.it

Abstract

In light chain amyloidosis (AL), fibrillar deposition of monoclonal immunoglobulin light chains (LCs) in vital organs, such as heart, is associated with their severe dysfunction. In addition to the cellular damage caused by fibril deposition, direct toxicity of soluble prefibrillar amyloidogenic proteins has been reported, in particular for cardiotoxicity. However, the molecular bases of proteotoxicity by soluble LCs have not been clarified. Here, to address this issue, we rationally engineered the amino acid sequence of the highly cardiotoxic LC H6 by introducing three residue mutations, designed to reduce the dynamics of its native state. The resulting mutant (mH6) is less toxic than its parent H6 to human cardiac fibroblasts and *C. elegans.* The high sequence and structural similarity, together with the different toxicity, make H6 and its non-toxic designed variant mH6 a test case to shed light on the molecular properties underlying soluble toxicity. Our comparative structural and biochemical study of H6 and mH6 shows closely matching crystal structures, whereas spectroscopic data and limited proteolysis indicate that H6 displays poorly cooperative fold, higher flexibility and kinetic instability, and a higher dynamic state in its native fold. Taken together, the results of this study show a strong correlation between the overall conformational properties of the native fold and the proteotoxicity of cardiotropic LCs.

Keywords: Light Chain amyloidosis, Proteotoxicity, Fold stability, Protein dynamics, Protein structure

INTRODUCTION

Amyloid diseases are characterized by the aberrant accumulation of misfolded proteins as amyloid fibrils in the interstitium of target organs[1, 2]. In the systemic forms, different organs can be involved, and amyloid deposition is associated with severe damage of the affected tissues. Defining the molecular features that predispose to amyloid formation, understanding the molecular bases of proteotoxicity and the mechanisms causing organ dysfunction are crucial steps for deciphering and treating these pathologic conditions. Protein misfolding and tissues damage are intuitively related processes, but the link between them remains unclear in many cases. In most amyloid related diseases, the presence of amyloid deposits *per se* is not considered sufficient to explain the clinical phenotype[3-8]. While the bulky extracellular deposits often alter the macro- and micro-architecture of organs, a direct cytotoxicity of soluble protein species has been firmly demonstrated for different amyloid diseases, including light chain (AL) amyloidosis[9-17].

AL amyloidosis is the most common form of systemic amyloidosis; it is caused by deposition of misfolding-prone monoclonal immunoglobulin light chains (LCs), produced in excess by a bone marrow plasma cell clone, and transported to target organs through blood[18]. AL amyloidosis is a polymorphic disease: the variability among LCs, caused by genetic rearrangement and somatic hypermutation, is such that virtually every monoclonal protein is unique in its amino acid sequence[19, 20]. AL clinical phenotype is also variable: most patients show multi-organ involvement at presentation[21]. Heart involvement is particularly frequent (~75% of cases) and dramatically worsens patients' prognosis [21-24].

LCs belong to two different isotypes, λ and κ, the former being more often amyloidogenic than the latter[25-27]. Overexpressed free λ LCs (*i.e.* not associated to the heavy chains to form full size immunoglobulins) assemble into homodimers. Each chain hosts two immunoglobulin domains [20, 28]: the N-terminal variable domain (VL, about 110 amino acids) is characterised by high sequence variability, especially in the three hypervariable complementarity determining regions (CDRs, about 110 amino acids). On the contrary, the sequence of the C-terminal constant domain (CL) is well conserved within each isotype.

The heterogeneity of monoclonal LCs creates a complex scenario, prompting a search for common traits among amyloidogenic LCs with distinct sequences. *In vitro,* VL domains from amyloidogenic LCs readily form fibrils, while the presence of the CL domain has a stabilising effect on the full-length LC and reduces its amyloidogenic propensity [29-32]. A recent report showed that full length LCs structures are highly comparable[20]. In full length LCs, stability only partially correlates with pathogenicity; in contrast, flexibility and susceptibility to protease cleavage are distinctive properties of amyloidogenic LCs, compared to non-amyloidogenic ones[20, 31-33]. However, even though the recent three-dimensional (3D) structures of AL fibrils extracted from the heart of an AL patient indicate that the fibrillar core is built solely by residues belonging to the VL domain [34, 35], the role of proteolysis as a trigger of amyloid formation or as a post-aggregation process remains to be established.

A growing body of clinical and experimental evidence indicates that tissue damage in AL amyloidosis is not only due to the deposited fibrils, but also to a toxic effect directly caused on target cells by soluble LC species[4, 10, 15, 16]. This concept, strongly

supported by clinical observations (*i.e.,* rapid amelioration of cardiac dysfunction biomarkers upon reduction of the circulating pathogenic LC with therapy[4]), is recapitulated by established experimental models of LC cardiotoxicity. Soluble cardiotropic amyloidogenic LCs not only affect the viability of human and rodent cardiac cells through oxidative stress, but they also impair protein homeostasis and alter mitochondrial function[11-13, 15, 16, 36]. In the nematode *Caenorhabditis elegans,* the administration of cardiotropic LCs causes a profound functional and structural pharynx damage considered an "ancestral heart". Such damage is associated with the production of reactive oxygen species (ROS) and mitochondria injury[10, 11]. Intriguingly, non-amyloidogenic LCs from multiple myeloma patients (M-LC) do not trigger significant toxic effects *in vitro* or *in vivo*[10].

While the biochemical and biophysical basis of LC amyloidogenicity have been extensively studied[29-31, 37-43], the molecular origins of the toxicity due to soluble LC species remain to be uncovered. In order to shed light on this crucial aspect, we hypothesized that a series of distinctive structural traits that characterize the amyloidogenic cardiotropic LCs – in particular their high conformational flexibility – are also linked to their cardiac toxicity. To prove such hypothesis, we rationally modified the sequence of a severely cardiotoxic LC by introducing three point mutations, designed to reduce its conformational dynamics and to mimic the properties of M-LCs.

Our results show that the toxicity of the mutant protein in cellular and animal models is significantly lower than that of the wild type LC; comparative structural and biochemical characterisations of the natural and engineered LCs indicate that fold

flexibility and kinetic instability are key properties underlying cardiotoxicity of LC soluble species.

RESULTS

Amyloidogenic λ light chains are predicted to have increased flexibility

In order to identify mutations capable of stabilising an amyloidogenic LC (A-LC), we implemented a strategy that combines phylogenetic analysis of disease-related LC sequences with atomistic calculations of stability-changes upon mutation. First, we selected all λ LCs with at least a complete VL sequence from the ALBASE repository of LC sequences[44]. This procedure resulted in 65 unique M-LC sequences and 236 A-LC sequences. Thirteen LC sequences that we previously characterized were also added to this set[20].

Before proceeding with the design, we tested whether the correlation between high conformational dynamics and pathogenicity, observed in our previous study on thirteen amyloidogenic cardiotropic LCs[20], also held within this larger dataset. To this end we employed two sequence-based predictors: the s2D method that predicts the equilibrium population of secondary structure elements[45], and the DynaMine predictor[46], which predicts backbone dynamics. Both predictors are trained on solution-based NMR data, and thus are best designed to recapitulate protein dynamics. The analysis revealed a statistically significant difference between the predicted conformational dynamics of A-LC and M-LC chains (**Figure S1a,b**), in agreement with our experimental observations on the smaller dataset[20]. A-LC sequences are predicted to host a lower equilibrium population of β-strand elements and lower backbone rigidity, thus implying increased overall conformational

dynamics. Furthermore, the H6 sequence[20], which is the target of our design, was predicted to be representative of the average degree of dynamics of A-LC sequences (**Figure S1**). It should, however, be noted that the difference in structural rigidity between A- and M-LCs previously observed on a set of thirteen LCs is overall significant even though not clear-cut for each individual LC[20]. As a result, the error associated with both computational predictors is likely to be comparable with the expected differences in structural dynamics, which is in keeping with the overlap between the two distributions shown in **Figure S1**.

As an additional control, we ran predictions of intrinsic solubility using CamSol[47-49]. In agreement with the experimental results obtained using thirteen LC sequences[20], no significant differences in predicted solubility were observed between A- and M-LC chains. The cardiotoxic[10] H6 LC is predicted to be slightly more soluble than average, suggesting that its aggregation propensity should not directly result from intrinsic low solubility/high aggregation propensities.

Rational design of a conformationally less flexible H6 mutant

In order to identify candidate mutations that may turn the toxic H6 LC into a non-toxic M-LC by restraining conformational dynamics, a multiple sequence alignment (MSA) of all M-LC sequences was performed, and the H6 sequence was added to it (see Materials and Methods). A long list of possible amino acid substitutions was then compiled by comparing the frequency of the H6 residues at each alignment position with those of amino acids from M-LC sequences. Mutations at a given position were long-listed if amino acids other than the one present in H6 were the most frequently found in M-LC sequences. Only mutations falling in the VL domain were taken into

account. The sequences of CL domains and of the CDRs loops were excluded because virtually identical in A and M-LCs, or because too variable among sequences, respectively.

As a second step, we submitted the crystal structure of the H6 LC dimer, together with the aforementioned MSA data, to the PROSS web server[50]. Using the Rosetta energy function, this server models all mutations with a favourable log-likelihood substitution score, as computed from the submitted MSA. PROSS then discards models predicted to be destabilising, and returns candidate stabilising models by applying seven energy thresholds to the Rosetta energy. The returned candidates were thus ranked according to the first energy threshold that selected them, with number one corresponding to most stabilising residue replacements (**Table 1**).

Finally, we employed the FoldX force field[51] to predict the folding free energy change upon mutation (ΔΔG) for each of the shortlisted mutations, as well as for all consensus mutations from the M-LCs MSA even if not suggested by PROSS. Indeed, a recent assessment showed that achieving high accuracy with such atomistic methods is still challenging, and the performance of different energy functions, such as Rosetta and FoldX, may vary in different ways depending on the type of substitution and its structural context[52]. We found a mild agreement between the Rosetta and FoldX predictions, with 5 out of 8 shortlisted mutations predicted to be stabilising by both energy functions (**Table 1**).

Our rational design procedure yielded three mutations: V47L, T70N and G75T (Chothia numbering: V46L, T69N and G74T). Each of the three mutations was selected because it is (*i*) predicted to be highly stabilising by FoldX (ΔΔG < -1 kcal/mol), (*ii*) stabilising by Rosetta, and (*iii*) commonly found in M-LC sequences (**Table 1**). The resulting triple H6

mutant (mH6) was thus cloned, expressed, and purified according to standard protocols[20]. All samples of H6 and mH6 used in the experiments below were SEC purified and purely dimeric (**Figure S2**).

The mH6 mutant displays reduced toxicity in cell and in vivo

In order to evaluate whether or not the engineered mutations modified the LC biological properties, we tested H6 and mH6 on human cardiac fibroblasts (hCF) and on the nematode *C. elegans*. Importantly the toxicity of soluble species and not of amyloid aggregates was assessed by these methods [10, 13].

We previously showed that exposure of cultured hCF to cardiotropic soluble LCs diluted in the culture medium affects cell viability[12]. In this study we tested viability/toxicity by two independent methods, MTT assay and ATP content evaluation. Based on both assays, we demonstrated that the toxic effects of the triple mutant mH6 are significantly lower than those of H6, when the two LCs are incubated with hCF for 24 hours (Figure 1A,B).

The ability of natively dimeric H6 and mH6 to affect the *C. elegans* pharyngeal function was evaluated by feeding nematodes for 2 h with 100 μg/ml of each LC[10]. The LC M7, a previously characterized non-amyloid and non-toxic LC [10], was used as negative control. As expected, the pharyngeal activity was significantly impaired in worms fed with H6 compared to vehicle (187 ± 5 and 230 ± 3 pumps/min, respectively) to an extent similar to that of hydrogen peroxide (180 ± 6 pumps/min) (**Figure 1C**). Conversely, mH6, similarly to M7, did not affect the pharyngeal function (243 ± 5 and 240 ± 2 pumps/min for mH6 and M7, respectively). The pharyngeal pumping

dysfunction caused by H6 was accompanied by a significant increase in mitochondrial ROS production, as indicated by the enhanced fluorescence of MitoSOX, a mitochondria-specific redox-sensitive fluorophore. No specific MitoSOX fluorescence was observed in the worms pharynx upon the administration of the vehicle or mH6 (**Figure 1C,D**).

Taken together, these data reveal that the three mutations engineered in mH6 significantly reduce H6 toxic phenotype.

Effects of mH6 mutations on the native fold and stability

Native fold and stability of SEC purified solution of H6 and mH6 dimers were studied using circular dichroism (CD) and fluorescence spectroscopy. H6 and mH6 chemical stability was investigated by measuring the red-shift of the intrinsic fluorescence emission peak. When the two proteins are incubated with increasing concentrations of urea a red shift of the emission peak wavelength and an increase of the fluorescence intensity are observed, as typical for LCs. The red shift of H6 emission peak in presence of urea shows a biphasic behaviour. A first transition takes place between 0 – 2 M urea, with an apparent midpoint concentration (Cm_{app}) of 0.87 ± 0.24 M (**Figure** 2A, blue line). Further increase in the denaturant concentration yields a second transition, which leads to the complete denaturation of H6, with a Cm_{app} of about 3.26 ± 0.19 M urea (**Figure** 2A, blue line). On the other hand, mH6 denaturation in the presence of urea shows a markedly cooperative behaviour, with a single transition between the folded and unfolded protein forms: the calculated Cm_{app} for this transition is 3.76 ± 0.15 M urea (**Figure** 2A, red line). These data show that the

triple mH6 mutant is more stable against urea denaturation than H6. It is worth mentioning that under native conditions (*i.e.* in the absence of urea) the wavelength of the emission peak of H6 is red-shifted compared to mH6 (**Figure** 2A), thus indicating that in H6 tryptophan residues experience a more polar environment, likely due to an increased exposure to solvent. This observation may be due to a more flexible assembly for H6 compared to mH6. Although all the described transitions are apparently not affected by kinetic or irreversible contributions (*i.e*. all the transitions are symmetrical around their respective inflection points, as expected in urea titration), the overall chemical unfolding was found to be not reversible, preventing the application of a thermodynamic analysis of the results.

In terms of secondary structure, firstly far-UV spectra for both proteins were recorded in order to assess their native fold states. As expected, both spectra displayed the typical features of β structure-rich proteins, with minima at 218 nm and intersections with zero at 208 nm (**Figure** 2B). Although the two spectra have similar shapes, the signal intensity in the mH6 spectrum was higher compared to that of H6 (minimum -5500 deg cm^2 $dmol^{-1}$ and -3400 deg cm^2 $dmol^{-1}$, respectively), indicating that mH6 has a higher secondary structure content than H6 in solution.

Then, we evaluated the effect of mutations on thermal stability. Thermal unfolding was monitored at 202 nm, during temperature increase up to 80 °C. In good agreement with the data obtained by urea titration, H6 thermal unfolding indicated a two-steps process (**Figure** 2C), with apparent melting temperatures (Tm_{app}, defined as the minimum of the first derivative) of 44.1 ± 1.0 and 55.0 ± 0.8 °C for the first and second transitions, respectively. mH6 thermal denaturation is single-step, with a

Tm_{app} of 54.1 ± 0.3 °C, closely matching the Tm_{app} of the second transition observed in H6.

In order to independently assess the tertiary structure thermal stability, fluorescence of 8-anilinonaphthalene-1-sulfonic acid (ANS) was monitored at increasing temperatures (**Figure** 2D); comparable Tm_{app} values were observed for H6 and mH6 (57.5 ± 0.5 °C and 56.7 ± 0.4 °C, respectively). As previously reported[20], Tm_{app} values determined by ANS fluorescence are slightly higher than those measured using CD spectroscopy. Such discrepancy may be caused by a delayed exposure of the hydrophobic core along the unfolding process, or may depend on the kinetics of ANS binding. Interestingly, the ANS initial fluorescence intensity was higher for H6 than for mH6 (101 and 62 AU, respectively), suggesting that at 20°C, under native conditions, hydrophobic patches in H6 are more solvent accessible than in mH6. In addition, ANS temperature ramps confirm that mH6 unfolds following a single-step cooperative process, whereas H6 shows a first structural rearrangement at around 45-50°C, followed by a main transition at higher temperature.

In summary, the spectroscopic data show that the three mutations engineered in mH6 do not affect the LC overall fold and lead to a mild increase in conformational stability relative to H6. However, crucially, they also suggest that the H6 fold is more flexible and less cooperative compared to mH6 under native (or sub-denaturing) conditions.

mH6 mutations do not alter its crystal structure

In order to assess whether V47L, T70N and G75T mutations triggered any conformational change in the LC fold, the crystal structure of mH6 was determined.

mH6 crystals belong to the monoclinc space group I121, with one mH6 homo-dimer per asymmetric unit, and diffracted to 2.1 Å resolution. The crystal structure was determined by molecular replacement using the H6 3D structure as search model (PDB code **5MUD**). Data collection and refinement statistics are reported in **TABLE 2**. Excellent and continuous electron density allowed modelling residues Q1-C215 and S2-C215 in chain A and B, respectively (**Figure 3A**). Only residues Q1 at the N-*terminus* of chain B and S216 at the C-*terminus* of both chains could not be modelled due to lack of electron density. The three mutated residues were clearly resolved and modelled in the electron density map.

The overall mH6 architecture is consistent with the canonical β-sandwich immunoglobulin fold, with a quaternary structure closely matching previously solved homo-dimeric LCs, and in particular that of H6[20, 28]. Remarkably, all six CDRs and the C-terminal inter-chain disulphide bond, between C215 A and C215 B, are clearly traceable in the electron density.

A careful structural comparison between H6 and mH6 shows that the three mutations do not introduce major structural differences between the cardiotoxic H6 and its mutant. Structural superposition of the dimeric mH6 and H6 models resulted in a Cα root mean square deviation (r.m.s.d.) of 0.34 Å over the entire structure (**Figure 3A**), indicating very high conservation of the tertiary and quaternary structures. The normalised B-factor profiles of the H6 and mH6 structures match closely (data not shown), ruling out specific effects caused by the mutations on protein flexibility. Typically, LC dimers display intrinsic sources of structure flexibility: the linker region connecting VL and CL domain makes their reciprocal orientation highly variable and LC crystal structures exhibit different relative orientation of VL/VL domains[53]. Even

though H6 and mH6 crystals grew under different chemical conditions, the resulting crystal packing and crystal symmetry are identical. As shown in **Table S1**, H6 and mH6 show very similar relative VL/CL and VL/VL orientations. Moreover, the CDR loops despite their inherent flexibility superpose very well.

All the mutations are located in the VL domains and are exposed on the protein surface, with the exception of L47 in chain B that appears to be partially buried in the VL-VL interface (**Figure 3A**). More specifically, residue 47 is located on β4, at the edge of the dimer interface; the V47L mutation introduces a bulkier hydrophobic side chain, which contributes to van der Waals interactions stabilising the mH6 dimer interface. Nevertheless, the overall interface areas for H6 and mH6 are highly comparable in the two structures (**Table S1**). Residues 70 and 75 are located on the β5-β6 loop and on β6, respectively (**Figure 3B**). Analysis of the H-bond intra-molecular network surrounding the mutation sites indicates that these are virtually identical in the H6 and mH6 structures (**Figure** 3B). However, N70 side chain in mH6 establishes an additional H-bond with N26, likely better linking these two loops together (**Figure 3B**-upper panel). No major changes in the backbone geometry are observed in the H6 and mH6 structures: Psi and Phi values for mutated residues are closely matching and fall in the preferred regions of the Ramachandran plot; in particular the Psi and Phi values for G75 and of T75 are virtually identical. However, the substitution of G75 to T likely results in a more rigid and stable β6 strand, as T residues have stronger propensity for β structures than G ones [54]; moreover they are characterised by a more geometrically restrained backbone and a branched Cβ. The above observations help rationalising the contribution of each of the three mutations in determining mH6 more cooperative fold and more rigid assembly compared to H6.

Overall, the above analysis indicates that the structures of H6 and mH6 match very closely and that the three mutations do not alter mH6 tertiary and quaternary structure.

mH6 mutations reduce conformational flexibility of the native state

The overall conformational flexibility of H6 and mH6 was probed by means of limited proteolysis using trypsin (Tr) and proteinase K (Pk), two proteases with very different proteolytic patterns. Typically, highly flexible substrate proteins are characterized by fast kinetics of proteolysis; on the contrary, slow proteolysis is typical of rigid and compact domains/proteins[55].

In the presence of Tr, H6 is proteolysed faster than mH6. After five minutes, uncleaved H6 is reduced to about 35% of the starting amount, while ~55% of mH6 is still uncleaved. Such different behavior disappears only towards the end of the experiment (180 min), when both samples are almost totally proteolysed (**Figure** 4). This trend is consistent, and even more pronounced, in the presence of Pk: H6 is totally cleaved after 120 minutes, while ~40% of mH6 is still full length after 180 minutes (**Figure** 4). It is noteworthy that both Tr and Pk cleavage of H6 yields to discrete bands ranging between 15-20 kDa. The major discrete fragments visible after H6 limited tryptic proteolysis were identified by 2D electrophoresis coupled with LC-MS/MS (**Figure S3**). The two most abundant fragments contain the C-terminal portion of VL and the CL domain and the CL alone, respectively. This observation indicates that CL domain is proteolysed with markedly slower kinetics compared to the highly flexible VL domain. On the contrary, in the case of mH6 no discrete fragments were detected,

suggesting that VL and CL domains possess similar sensitivity to proteolysis (**Figure** 4). In all the above experiments, SEC-purified H6 and mH6 dimeric solutions were employed.

Taken together, these results show that mH6 is more resistant than H6 to proteolysis, suggesting that a marked decrease in protein flexibility was conferred by the mH6 engineered mutations.

Comparison of the unfolding kinetics of H6 and mH6

Unfolding kinetics of H6 and mH6 dimers were assessed in stopped-flow experiments at three different temperatures (20, 25, and 30 °C). Intrinsic fluorescence intensities have been recorded upon mixing protein samples with urea at a final denaturing concentration of 5 M (**Figure** 5A and 5B). The time-course unfolding traces fit to a first-order kinetic equation for both proteins, indicating the absence of major kinetic intermediates. At each tested temperature, H6 displays a faster unfolding compared to mH6. For example, at 20°C the apparent rate constants (k) are 0.075 ± 0.005 sec^{-1} and 0.041 ± 0.003 sec^{-1} for H6 and mH6, respectively, corresponding to a transition half-life time ($t_{1/2}$, the time required to halve the population of native protein) almost double for mH6 compared to H6 (16.90 and 9.24 sec, respectively). The different unfolding rates measured for H6 and mH6 are in keeping with their different flexibility under native conditions.

To better address the different kinetic behaviour, the activation energies of H6 and mH6 chemical unfolding (*i.e.* the free energy barrier that should be overcome from the native to the unfolded state in 5 M urea) have been calculated from the Arrhenius

plot reported in **figure 5C**. H6 shows a lower Ea compared to mH6 (906 ± 114 J/mol and 1041 ± 120 J/mol, respectively). Despite the low statistical significance (p-value 0.152 from a 2-tailed t-test), these results help to rationalise the different unfolding kinetics. The lower unfolding activation energy of H6 could be due either to a lower free energy level of its transition state or, more likely considering its marked flexibility, to a higher free energy level of its native state.

DISCUSSION

The identification of the molecular determinants of LC proteotoxicity and of the link between amyloidogenicity and toxicity is a crucial requirement to understand the pathological processes underlying AL amyloidosis, and to design therapeutic strategies counteracting organ damage. Although the toxicity of soluble LC dimers, or of small aggregates, is now considered a key factor determining heart damage in AL patients[6], the molecular determinants of such toxicity have not been investigated and remain unclear. Our study focused on filling this gap, by testing the existence of relationship between LC's biophysical/biochemical properties and proteotoxicity.

To this end, H6, a λ LC responsible for severe cardiotoxicity, and representative of the previously analysed group of amyloidogenic cardiotropic LCs[20], was selected. A rational design approach aimed at increasing conformational stability led us to design a LC triple mutant by engineering mutations that are conservative in terms of residue charge, hydrophobicity and steric hindrance. To avoid the disruption of H6 structure or assembly, the selected mutations are located on the protein surface, while regions expected to grossly modify the biochemical properties, such as the hydrophobic core

or dimer interface, were left untouched. As a first functional result, the engineered mH6 mutant was proven to be less toxic *in vitro* to human cardiac fibroblasts compared to H6. In *C. elegans,* where ROS generated by cardiotoxic LCs, such as H6, cause an injurious oxidative stress to pharyngeal cells[10, 11], the effect of mH6 on the feeding behavior and mitochondrial damage was comparable to that of the non-toxic M7 LC.

The biophysical features of mH6 are fully comparable with H6 in terms of properties due to the protein sequence (predicted solubility and hydrophobicity) and, in keeping with the goals of the design, the crystal structure confirmed that the mutations have no significant structural effects. H6 and mH6 tertiary and quaternary structures proved virtually identical, ruling out the possibility that toxicity reduction might come from major modifications of the H6 structural assembly.

Thus, the high sequence and structural similarities, together with the different toxicities, make H6 and its non-toxic variant mH6 an ideal test case to shed light on the molecular properties underlying LC soluble toxicity.

The comparative biophysical characterisation of H6 and mH6 disclosed notable differences between the toxic and the non-toxic variant. While the two proteins display broadly comparable Cm_{app} and Tm_{app} values, as assessed by chemical and thermal denaturation, several lines of evidence indicate that H6 and mH6 behaviours in solution bear crucial differences. A poorly cooperative unfolding, a low CD signal, the exposure of hydrophobic patches under native conditions and susceptibility to proteolysis, are together strong indicators that H6 is characterised by a flexible native state, with looser secondary and tertiary structures in comparison to mH6. Moreover,

faster H6 unfolding kinetics suggests that mH6 is kinetically more stable. Thus, the *in vitro* and *in vivo* data link H6 toxicity with protein flexibility and kinetic instability. Additionally, some of our biophysical data may provide further insight: a two-step unfolding process and the fast and abundant fragmentation at the beginning of the H6 proteolytic reaction are compatible with a highly dynamic native-like state, characterised by low fold stability and loose tertiary structure (**Figures 2 and 4**). Such state would also explain the lower intensity of the CD signal of H6, stronger ANS fluorescence, and the red-shifted intrinsic fluorescence maximum under native conditions compared to mH6 (**Figure 2**).

As a whole, the biophysical properties correlating with soluble toxicity of this pair of LCs are comparable with those reported by us and others for LC amyloidogenicity. Indeed protein flexibility seems to be connected with LC amyloidogenicity [20, 31, 32], kinetic instability has been observed in several amyloidogenic LCs [29, 31, 33, 56], while chemical and thermal stabilities are not *per se* necessarily prognostic, though often correlated with the aggregation propensity [20, 30, 57, 58]. Molecules stabilising LC native state may not only be used as inhibitors of amyloid formation but also to lower LC soluble proteotoxicity[59, 60].

Although amyloidogenic LCs display toxicity to target organs also in soluble form, amyloid deposits are always found in affected organs in AL, suggesting the existence of a link between amyloidogenicity and soluble proteotoxicity. However, it remains to be understood whether such properties are two pathologic behaviours intrinsically triggered by the same molecular features, or whether they coexist because protein instability is a necessary trait for both phenomena. In this respect, a thorough

investigation of the biophysical properties related to soluble proteotoxicity and not to aggregation propensity is of particular interest. Given the high sequence variability typical of LCs involved in AL, we believe that the first approach to deliver generalizable data should be to shift the research focus from the role of specific residues in LC sequences to the biophysical characterisation of pathogenic LCs.

To date, especially in neurodegenerative amyloid-related diseases oligomers are considered the main source of toxicity [61]. Although a direct involvement of LC oligomers in AL has not been proven, a key role of the soluble forms in the toxicity has been demonstrated[10]. Specifically the data here presented do not identify the molecular LC species directly responsible for proteotoxicity: full length LC dimers (misfolded or unfolded), transient oligomers (as suggested for other amyloid diseases)[61], or proteolysed LC fragments (abundant components of *ex-vivo* amyloid fibrils) may be the soluble species generating cell damage. In fact, our results are still compatible with different scenarios. *In vitro,* H6 is quickly proteolysed: *in vivo* fast proteolysis may release toxic peptides. Alternatively, the partial exposure of hydrophobic patches under native conditions, the marked protein flexibility and kinetic instability observed for H6 may promote the formation of non-native toxic oligomers.

In summary, the successful design of a variant of a highly cardiotoxic LC that displays significantly lower toxicity, offered us the unique opportunity to elucidate the biophysical and biochemical properties correlating with LCs soluble toxicity. Even though the precise mechanisms by which the proteotoxic LC soluble species interact with cells and cause toxicity are still unclear, the present data lead the way to clarify

the molecular basis of this phenomenon. Moreover, our findings suggest a strategy to tackle cardiotoxicity in AL amyloidosis: ligand molecules able to rigidify and kinetically stabilise the LC dimeric fold would, in turn, promptly lower LC soluble toxicity.

MATERIALS AND METHODS

Rational design of mH6

The sequences of VL domains of λ LC were downloaded from the ALBASE repository, and only complete sequences with no unknown 'X' amino acids were retained, which resulted in 65 unique M-LC sequences and 236 unique A-LC sequences. The multiple sequence alignment (MSA) of the M-LC sequences was carried out with the *anarci* python software[62], using the Chothia residue numbering scheme. The sequence of the H6 LC was added to this alignment in the same way. This MSA was used as input to the PROSS web server [50] (pross.weizmann.ac.il) together with the crystal structure of the H6 dimer (PDB ID **5MUD**), which was the object of the PROSS optimisation procedure. Residues belonging to the CDRs and to the constant region were excluded from the design. FoldX version 4 was downloaded from foldxsuite.crg.eu [51] and the shortlisted mutations were run onto the H6 dimer crystal structure according to user instructions. Three runs were carried out per mutation, and the input pdb file was first optimised with the *foldx -c optimize* command.

Mutagenesis, expression and purification

Site-directed mutagenesis of the H6 gene (GeneBank code: **KY471433**) was performed using QuikChange Lightning Site-Directed Mutagenesis Kit (Agilent Technologies). Synthetic oligonucleotide primers were designed using the online tool QuikChange® Primer Design (www.genomics.agilent.com/primerDesignProgram.jsp). Specifically,

V47L Fw: 5'-TTTT CATACATGATGAGTTTGGGGGTTCTTCCTGGG-3'

Rv: 5'-CCCAGGAAGAACCCCCAAA CTCATCATGTATGAAAA-3';

T70N: Fw: 5'-AGGGTGGCTGAATTGCCAGACTTGGAGCC AGAG-3'

Rv: 5'-CTCTGGCTCCAAGTCTGGCAATTC AGCCACCCT-3'

G75T: Fw: 5'-GGAGTCCGGTGATGGTCAGGGTGGCTGACG-3'

Rv: 5'-CGTCAGCCACCCTGACCAT CA CCGGACTCC-3'.

Polymerase Chain Reaction (PCR) mix was performed following the manufacturer's instructions. The successful mutagenesis was verified through the automated Sanger sequencing platform provided by Eurofins Genomics (https://www.eurofinsgenomics.eu). mH6, H6 and M7 were expressed and purified according to previously reported protocols[20].

Effect of LC on cardiac fibroblasts and C. elegans

Primary cardiac fibroblasts (hCFs) from normal human adult heart were purchased from the European Collection of Cell Cultures (Public Health England, #306-05A), and cultured in medium with fetal bovine serum (FBS) as previously described[13]. For viability assays, cells (used at passage n. 4) were seeded in 96-wells plates at a density of 5,000 cells/well and exposed for 24 h to 5 µM of each LC diluted in Opti-MEM medium (Gibco, Thermo Fisher Scientific, Waltham, MA, USA) without FBS. Cell viability/toxicity was measured using 3-(4,5-Dimethylthiazol-2-yl)-2,5-

Diphenyltetrazolium Bromide (MTT) (Pierce, Thermo Fisher Scientific, Waltham, MA, USA) and by ATP content evaluation. For the MTT assay, after incubation with LCs, the medium was carefully removed, followed by addition of 100 µl of Opti-MEM and 10 µl of MTT solution (5 mg/ml in PBS) to each well. After 3 h of incubation at 37°C, 100 µl of MTT solution (1:1 ethanol:DMSO) were added. Absorbances at 570 nm (FI1) and 650 nm (FI2) were measured with a microplate reader (Infinite F200, Tecan); FI1-FI2 was calculated. Relative cell viability (%) was calculated using control wells containing hCFs grown in standard growth medium (untreated) as reference condition. For ATP measurement, hCF were seeded in white opaque-walled 96-wells plates and exposed to LCs as indicated above. After incubation, the medium was carefully removed and replaced with 100 µl of fresh Opti-MEM medium, without washing. The ATP content of cells exposed to LC and controls was assessed using CellTiter-Glo Luminescent Cell Viability Assay (Promega, Madison, Wisconsin, USA), according to the manufacturer's protocol. Briefly, 100 µl of CellTiter-Glo® Reagent was added in each well, followed by 10 min incubation at room temperature, with shaking. Luminescent signals (RLU) were recorded on a microplate reader (Infinite F200, Tecan). The experiments were performed using five biological replicates in two technical replicates.

Bristol N2 nematodes were obtained from the *C. elegans* Genetic Center (CGC; University of Minnesota, Minneapolis, USA) and propagated at 20°C on solid Nematode Growth Medium (NGM) seeded with OP50 *E. coli* (CGC; University of Minnesota, Minneapolis, USA) for food. Worms were fed LC as previously described[10]. Age-synchronized L3 worms were collected with M9 buffer, centrifuged at 290 x *g* for 3 min at room temperature and washed three times with 10 mM PBS, pH 7.4, to completely remove bacteria. Nematodes were fed with 100 µg/ml

H6, mH6 or M7 (100 worms/100 µl). Worms fed 10 mM PBS, pH 7.4, alone (Vehicle) or 1 mM H_2O_2 as positive control. After 2 h incubation, worms were transferred onto fresh NGM plates seeded with OP50 *E. coli* and incubated at 20°C. The pharyngeal pumping rate, measured by counting the number of times the terminal bulb of the pharynx contracted over a 1-minute interval (pumps/min), was measured 24 h later[10].

The effect of LC administration on *in vivo* mitochondrial oxidant burden, was also evaluated. To this end, 2 h after feeding of H6, mH6 or M7, worms were moved onto NGM plates seeded with fresh bacteria as food and 10 µM MitoSOX Red (Molecular Probes, Italy)[10]. Twenty-four hours later, nematodes were collected, centrifuged at 290 *x g* for 3 min and washed twice with M9 buffer to eliminate bacteria. Worms were then transferred onto fresh NGM plates seeded with OP50 and left for 1 h to remove the residual dye from the pharynx lumen[11]. After collecting and washing them with M9 buffer, nematodes were paralyzed with 20 mM levamisole (Sigma-Aldrich) and fixed for 24 h at 4°C in 4% paraformaldehyde before the epifluorescence analysis (IX-71 Olympus equipped with a CDD camera).

Intrinsic fluorescence.

Chemical stability of the tertiary structure of H6 and mH6 was evaluated by measuring changes in the intrinsic protein fluorescence in presence of increasing urea concentrations. H6 and mH6 were diluted at a concentration of 0.1 mg/mL, in 10 mM sodium phosphate buffer, pH 7.4, with increasing concentrations of denaturant. Fluorescence emission spectra from 300 to 450 nm were recorded at 20°C, following 5-minutes incubation, in a LS 50 spectrofluorimeter (Perkin Elmer); excitation

wavelength 284 nm. Titrations were repeated in triplicates. Protein denaturation has been assessed by plotting the wavelength of the fluorescence emission peak as a function of denaturant concentration. Lines represent the best fit for the data. Experimental data were fitted with a sigmoid equation (4 parameters).

Circular dichroism.

Circular dichroism experiments, in the Far- and Near-UV regions, were carried out on a J-810 spectropolarimeter (JASCO Corp., Tokyo, Japan) equipped with a Peltier system for temperature control. All experiments were performed in triplicates and were carried out in 50 mM sodium phosphate pH 7.4. For the experiments in Far-UV region we used 200 µL of 0.2 mg/ml LCs in a cuvette with a path length of 0.1 cm. Spectra were recorded from 260 to 190 nm and normalized in term of mean residue ellipticity (MRE). Temperature ramps were monitored at 202 nm for 1 hour. Temperature increased from 20 to 80 °C with a 60 °C/hour temperature slope. Spectra and temperature ramps were performed in triplicate for each LC. Tm_{app} was calculated as the first-derivative minimum of the temperature ramps.

ANS fluorescence.

ANS fluorescence temperature ramps were performed in 50 mM sodium phosphate pH 7.4, at 0.1 mg/ml protein concentration, in the presence of 100 µM ANS. Experiments were performed in triplicates. Fluorescence intensity was monitored at 490 nm in a 1 cm path length cuvette while temperature increased from 20 to 80 °C (temperature slope 60 °C/hour). Excitation and Emission slits were set at 5 nm. Tm_{app} was calculated as the first-derivative minimum of the temperature ramps.

Crystallization and structure determination

Protein solution of mH6 in 50 mM sodium phosphate buffer pH 7.4 was concentrated to 8 mg/ml. Crystals of mH6 were obtained at 20 °C using the sitting drop technique from a 2:1 mixture of protein and reservoir solution (drop volume 0.3 µL). Crystals of mH6 grew in 0.02 M sodium/potassium phosphate, 0.1 M Bis Tris propane pH 8.5, 20% w/v PEG 3350 (PACT premier™, Molecular Dimensions), and were cryoprotected by adding 33% glycerol to mother liquor and then flash frozen in liquid nitrogen. X-ray diffraction experiments were performed at the ESRF (European Synchrotron Radiation Facility in Grenoble, France), ID29 beam line. Data were analyzed and processed using XDS [63]. mH6 crystal structure was solved by molecular replacement using MolRep [64] using the H6 structure as search model (PDB: 5MUD). Manual building and refinement of mH6 structure were performed using Coot [65], Phenix Refine [66] and Buster [67]; for X-ray data collection and refinement statistics see Table 2. The stereochemistry and the agreement between the model and the X-ray data were verified by Coot and MolProbity [65, 68]. The secondary structure matching (SSM) algorithm of Coot was used to perform structural superpositions of mH6 and H6. VL/VL orientation was calculated and analyzed using ABangle[53]. Protein-protein interface area calculations were performed using the Protein Interfaces, Surfaces and Assemblies service (PISA) available at the European Bioinformatics Institute (http://www.ebi.ac.uk/msd-srv/prot_int/pistart.html) [69]. The network of non-covalent bonds within H6 and mH6 crystal structures were mapped through RING 2.0 web server[70]. Figure 3 was generated using PyMOL (http://www.pymol.org).

Limited proteolysis.

LCs at a concentration of 1 mg/ml, were incubated with a bovine trypsin (Sigma Aldrich) or Proteinase K (Genespin) at 37 °C in 50mM sodium phosphate at pH 7.4 and samples were collected at different time points (0' 10', 20', 30', 60', 90', 120', 150', 180'). For trypsin experiments, 1 M urea was added to the final mix. The molar ratio protease/protein was 1:100 for trypsin and 1:150 for Proteinase K. Each sample was diluted in denaturating and reducing sample buffer (NuPAGE, Invitrogen). Then, they were heated for 3 min at 95 °C and analyzed by SDS-PAGE. The uncleaved protein fraction was quantified by densitometry using Chemidoc™ MP System (Bio-Rad).

Stopped-flow

The unfolding rates in urea of H6 and mH6 were studied by stopped-flow fluorescence. Measurements were carried out at three temperatures (20, 25 and 30 °C) by using a SFM20 stopped-flow apparatus (BioLogic, France) with a four-optical surface and 2 mm path length quartz cell. The stopped-flow apparatus was attached to a J810 spectropolarimeter set at 284 nm (excitation wavelength) and equipped with a fluorescent detector set at 370 nm (emission wavelength) placed orthogonally to the CD light beam. The unfolding kinetics were monitored for 200 sec on a 0.2 mg/mL protein solution at 5 M urea (*i.e.* a denaturing urea concentration for both H6 and mH6). In details, 112.5 μL of a 0.533 mg/m protein sample were mixed in 200 msec with 187.5 μL of urea 8M (instrumental dead time 39.5 msec). The observed changes, *i.e.,* the increase in emitted fluorescence at 370 nm, were fitted to a first-order kinetic equation (exponential rise to maximum) (1).

$$F_t = F_0 + F_{max} (1-e^{-kt}) \quad (1)$$

Where F_t, F_0 and F_{max} are the intensity of emitted fluorescence at time "t", at time "zero", and at infinite time after the mixing, respectively; k is the apparent first-order rate constant of the observed change.

The activation energies of H6 and mH6 chemical unfolding were calculated from the slopes of the respective Arrhenius plots (2), in which the natural logarithms of the rate constants (ln k) are plotted *versus* the reciprocal of the temperature in Kelvin (1/T)

$$\ln k = \ln A - (Ea/R)(1/T) \quad (2)$$

Where "k" is the apparent first-order rate constant, "A" the pre-exponential factor, "Ea" the activation energy, "R" the gas constant, and "T" the temperature in Kelvin.

Accession numbers

mH6 atomic coordinates and the structure factors have been deposited in the Protein Data Bank with the following accession number: 6GRZ.

Acknowledgements

We thank Maria Monica Barzago for her support in *C. elegans* experiments. This work was supported by the Italian Ministry of Health (RF-2013-02355259 and RF-2016-02361756); by Fondazione Cariplo (grants n. 2013–0964, 2015-0591 and 2016-0489); Italian Medicines Agency (grant AIFA-2016-02364602), the European Union (E-Rare

JTC 2016 grant ReDox, by Fondazione ARISLA (project TDP-43-STRUCT) and by Fondazione Telethon (GGP17036). *C. elegans* and OP50 *E. coli* were provided by the GCG, which is funded by NIH Office Research Infrastructure Programs (P40 OD010440).

Figure Legends:

Figure 1. mH6 displays low soluble toxicity compared to H6. A) Effect of H6 and mH6 on viability of cultured human cardiac fibroblasts, evaluated using MTT assay. Data are expressed as values normalized on the mean of untreated cells (vehicle) **** $p<0.001$; °° $p<0.05$ (two technical replicates). B) ATP content in hCF exposed to H6 and mH6, measured by luminescence. °° $p<0.05$. C) Worms were fed for 2 h with 100 µg/ml H6, mH6 or M7. Control worms were incubated with 10 mM PBS, pH 7.4 (Vehicle) or 1 mM H_2O_2 as positive control. Pumping rate as mean pumps/min ± SE (n = 20 worms/assay, three assays). ****$p < 0.001$ *vs* vehicle, °°°°$p < 0.001$ *vs* mH6, one-way ANOVA and Bonferroni's *post hoc* test. D) Images obtained from the overlay of a contrast phase and MitoSOX fluorescence (arrows). Scale bar 50 µm.

Figure 2. Effects of the mH6 mutations on the native structure and stability. A) Chemical stability of H6 (blue) and mH6 (red). The wavelength of the intrinsic fluorescence emission peak has been plotted as a function of urea concentration. Lines represent the best fit for the data. Experimental data were fitted with a sigmoid equation (4 parameters). B) Far-UV CD spectrum for H6 (blue curve) and mH6 (red curve); C) Representative temperature ramps monitored by Far-UV CD for H6 (blue curve) and mH6 (red curve) recorded at 202 nm while temperature was increased up to 80 °C. D) Representative temperature ramps monitored by ANS fluorescence for H6 (blue curve) and mH6 (red curve) monitored at 490 nm while the temperature was increased up to 80 °C.

Figure 3. Crystal structure of mH6. A) Cartoon representation of the mH6 dimer (both chains A and B red) superposed onto H6 structure (blue). B) Zoom into the local environment of the three mutation sites: mutated amino acids and the adjacent residues are shown as sticks, wild type and mutated residues are blue and green, respectively.

Figure 4. The mH6 mutations reduce the conformational flexibility of the native state. A) Limited proteolysis SDS-PAGE analyses. Top panels: H6 (left) and mH6 (right) incubated with Pk. Bottom panels: H6 (left) and mH6 (right) incubated with Tr. In each gel, molecular markers (MM) were loaded first, followed by the protease (Pk or Tr), the native protein and samples after 1, 5, 10, 15, 20, 30, 60, 120 and 180 minutes protease incubation. B) H6 (blue lines) and mH6 (red lines) Trypsin (dashed lines) and Proteinase K (continuous lines) limited proteolysis kinetics. Values were obtained quantifying the uncleaved protein fraction by densitometry on the gels.

Figure 5. **Unfolding kinetics of H6 and of mH6.** Unfolding kinetics of H6 (A) and mH6 (B) in urea 5M at three temperatures. The curves are the average of three

independent experiments. Changes in tryptophan fluorescence emission at 370 nm were fitted to a first-order exponential kinetic equation (black lines).

REFERENCES:

[1] Benson MD, Buxbaum JN, Eisenberg DS, Merlini G, Saraiva MJM, Sekijima Y, et al. Amyloid nomenclature 2018: recommendations by the International Society of Amyloidosis (ISA) nomenclature committee. Amyloid : the international journal of experimental and clinical investigation : the official journal of the International Society of Amyloidosis. 2018;25:215-9.

[2] Nuvolone M, Merlini G. Systemic amyloidosis: novel therapies and role of biomarkers. Nephrology, dialysis, transplantation : official publication of the European Dialysis and Transplant Association - European Renal Association. 2017;32:770-80.

[3] Madhivanan K, Greiner ER, Alves-Ferreira M, Soriano-Castell D, Rouzbeh N, Aguirre CA, et al. Cellular clearance of circulating transthyretin decreases cell-nonautonomous proteotoxicity in Caenorhabditis elegans. Proc Natl Acad Sci U S A. 2018;115:E7710-E9.

[4] Palladini G, Lavatelli F, Russo P, Perlini S, Perfetti V, Bosoni T, et al. Circulating amyloidogenic free light chains and serum N-terminal natriuretic peptide type B decrease simultaneously in association with improvement of survival in AL. Blood. 2006;107:3854-8.

[5] Reixach N, Deechongkit S, Jiang X, Kelly JW, Buxbaum JN. Tissue damage in the amyloidoses: Transthyretin monomers and nonnative oligomers are the major cytotoxic species in tissue culture. Proc Natl Acad Sci U S A. 2004;101:2817-22.

[6] Sapp V, Jain M, Liao R. Viewing Extrinsic Proteotoxic Stress Through the Lens of Amyloid Cardiomyopathy. Physiology. 2016;31:294-9.

[7] Schonhoft JD, Monteiro C, Plate L, Eisele YS, Kelly JM, Boland D, et al. Peptide probes detect misfolded transthyretin oligomers in plasma of hereditary amyloidosis patients. Science translational medicine. 2017;9.

[8] Eisele YS, Janssen ME, MA D, Nguyen B, Plate L, Morgan GJ, et al. FORMATION AND TOXICITY OF TRANSTHYRETIN (TTR) OLIGOMERS IN VITRO AND IN PATIENTS WITH FAMILIAL AMYLOID POLYNEUROPATHY. Alzheimer's & Dementia: The Journal of the Alzheimer's Association, . 2018;14:1123-4.

[9] Brenner DA, Jain M, Pimentel DR, Wang B, Connors LH, Skinner M, et al. Human amyloidogenic light chains directly impair cardiomyocyte function through an increase in cellular oxidant stress. Circ Res. 2004;94:1008-10.

[10] Diomede L, Rognoni P, Lavatelli F, Romeo M, Del Favero E, Cantu L, et al. A Caenorhabditis elegans-based assay recognizes immunoglobulin light chains causing heart amyloidosis. Blood. 2014.

[11] Diomede L, Romeo M, Rognoni P, Beeg M, Foray C, Ghibaudi E, et al. Cardiac Light Chain Amyloidosis: The Role of Metal Ions in Oxidative Stress and Mitochondrial Damage. Antioxidants & redox signaling. 2017;27:567-82.

[12] Imperlini E, Gnecchi M, Rognoni P, Sabido E, Ciuffreda MC, Palladini G, et al. Proteotoxicity in cardiac amyloidosis: amyloidogenic light chains affect the levels of intracellular proteins in human heart cells. Sci Rep. 2017;7:15661.

[13] Lavatelli F, Imperlini E, Orru S, Rognoni P, Sarnataro D, Palladini G, et al. Novel mitochondrial protein interactors of immunoglobulin light chains causing heart amyloidosis. FASEB journal : official publication of the Federation of American Societies for Experimental Biology. 2015;29:4614-28.

[14] Liao R, Jain M, Teller P, Connors LH, Ngoy S, Skinner M, et al. Infusion of light chains from patients with cardiac amyloidosis causes diastolic dysfunction in isolated mouse hearts. Circulation. 2001;104:1594-7.

[15] Marin-Argany M, Lin Y, Misra P, Williams A, Wall JS, Howell KG, et al. Cell Damage in Light Chain Amyloidosis: FIBRIL INTERNALIZATION, TOXICITY AND CELL-MEDIATED SEEDING. J Biol Chem. 2016;291:19813-25.
[16] Shi J, Guan J, Jiang B, Brenner DA, Del Monte F, Ward JE, et al. Amyloidogenic light chains induce cardiomyocyte contractile dysfunction and apoptosis via a non-canonical p38alpha MAPK pathway. Proc Natl Acad Sci U S A. 2010;107:4188-93.
[17] Sikkink LA, Ramirez-Alvarado M. Cytotoxicity of amyloidogenic immunoglobulin light chains in cell culture. Cell Death Dis. 2010;1:e98.
[18] Merlini G, Dispenzieri A, Sanchorawala V, Schonland SO, Palladini G, Hawkins PN, et al. Systemic immunoglobulin light chain amyloidosis. Nature reviews Disease primers. 2018;4:38.
[19] Kourelis TV, Dasari S, Theis JD, Ramirez-Alvarado M, Kurtin PJ, Gertz MA, et al. Clarifying immunoglobulin gene usage in systemic and localized immunoglobulin light-chain amyloidosis by mass spectrometry. Blood. 2017;129:299-306.
[20] Oberti L, Rognoni P, Barbiroli A, Lavatelli F, Russo R, Maritan M, et al. Concurrent structural and biophysical traits link with immunoglobulin light chains amyloid propensity. Sci Rep. 2017;7:16809.
[21] Merlini G, Wechalekar AD, Palladini G. Systemic light chain amyloidosis: an update for treating physicians. Blood. 2013;121:5124-30.
[22] Merlini G, Palladini G. Light chain amyloidosis: the heart of the problem. Haematologica. 2013;98:1492-5.
[23] Palladini G, Dispenzieri A, Gertz MA, Kumar S, Wechalekar A, Hawkins PN, et al. New criteria for response to treatment in immunoglobulin light chain amyloidosis based on free light chain measurement and cardiac biomarkers: impact on survival outcomes. J Clin Oncol. 2012;30:4541-9.
[24] Vaxman I, Gertz M. Recent Advances in the Diagnosis, Risk Stratification, and Management of Systemic Light-Chain Amyloidosis. Acta haematologica. 2019;141:93-106.
[25] Comenzo RL, Wally J, Kica G, Murray J, Ericsson T, Skinner M, et al. Clonal immunoglobulin light chain variable region germline gene use in AL amyloidosis: association with dominant amyloid-related organ involvement and survival after stem cell transplantation. British journal of haematology. 1999;106:744-51.
[26] Dasari S, Theis JD, Vrana JA, Meureta OM, Quint PS, Muppa P, et al. Proteomic detection of immunoglobulin light chain variable region peptides from amyloidosis patient biopsies. Journal of proteome research. 2015;14:1957-67.
[27] Perfetti V, Casarini S, Palladini G, Vignarelli MC, Klersy C, Diegoli M, et al. Analysis of V(lambda)-J(lambda) expression in plasma cells from primary (AL) amyloidosis and normal bone marrow identifies 3r (lambdaIII) as a new amyloid-associated germline gene segment. Blood. 2002;100:948-53.
[28] Bourne PC, Ramsland PA, Shan L, Fan ZC, DeWitt CR, Shultz BB, et al. Three-dimensional structure of an immunoglobulin light-chain dimer with amyloidogenic properties. Acta Crystallogr D Biol Crystallogr. 2002;58:815-23.
[29] Blancas-Mejia LM, Horn TJ, Marin-Argany M, Auton M, Tischer A, Ramirez-Alvarado M. Thermodynamic and fibril formation studies of full length immunoglobulin light chain AL-09 and its germline protein using scan rate dependent thermal unfolding. Biophysical chemistry. 2015;207:13-20.
[30] Klimtchuk ES, Gursky O, Patel RS, Laporte KL, Connors LH, Skinner M, et al. The critical role of the constant region in thermal stability and aggregation of amyloidogenic immunoglobulin light chain. Biochemistry. 2010;49:9848-57.

[31] Morgan GJ, Kelly JW. The kinetic stability of a full-length antibody light chain dimer determines whether endoproteolysis can release amyloidogenic variable domains. J Mol Biol. 2016.
[32] Weber B, Hora M, Kazman P, Gobl C, Camilloni C, Reif B, et al. The Antibody Light-Chain Linker Regulates Domain Orientation and Amyloidogenicity. J Mol Biol. 2018.
[33] Morgan GJ, Usher GA, Kelly JW. Incomplete Refolding of Antibody Light Chains to Non-Native, Protease-Sensitive Conformations Leads to Aggregation: A Mechanism of Amyloidogenesis in Patients? Biochemistry. 2017;56:6597-614.
[34] Radamaker L, Lin YH, Annamalai K, Huhn S, Hegenbart U, Schonland SO, et al. Cryo-EM structure of a light chain-derived amyloid fibril from a patient with systemic AL amyloidosis. Nature communications. 2019;10:1103.
[35] Swuec P, Lavatelli F, Tasaki M, Paissoni C, Rognoni P, Maritan M, et al. Cryo-EM structure of cardiac amyloid fibrils from an immunoglobulin light chain (AL) amyloidosis patient. bioRxiv. 2018.
[36] Guan J, Mishra S, Qiu Y, Shi J, Trudeau K, Las G, et al. Lysosomal dysfunction and impaired autophagy underlie the pathogenesis of amyloidogenic light chain-mediated cardiotoxicity. EMBO molecular medicine. 2014;6:1493-507.
[37] Blancas-Mejia LM, Hammernik J, Marin-Argany M, Ramirez-Alvarado M. Differential effects on light chain amyloid formation depend on mutations and type of glycosaminoglycans. J Biol Chem. 2015;290:4953-65.
[38] Blancas-Mejia LM, Misra P, Dick CJ, Cooper SA, Redhage KR, Bergman MR, et al. Immunoglobulin light chain amyloid aggregation. Chemical communications. 2018;54:10664-74.
[39] Blancas-Mejia LM, Tellez LA, del Pozo-Yauner L, Becerril B, Sanchez-Ruiz JM, Fernandez-Velasco DA. Thermodynamic and kinetic characterization of a germ line human lambda6 light-chain protein: the relation between unfolding and fibrillogenesis. J Mol Biol. 2009;386:1153-66.
[40] del Pozo Yauner L, Ortiz E, Sanchez R, Sanchez-Lopez R, Guereca L, Murphy CL, et al. Influence of the germline sequence on the thermodynamic stability and fibrillogenicity of human lambda 6 light chains. Proteins. 2008;72:684-92.
[41] del Pozo-Yauner L, Wall JS, Gonzalez Andrade M, Sanchez-Lopez R, Rodriguez-Ambriz SL, Perez Carreon JI, et al. The N-terminal strand modulates immunoglobulin light chain fibrillogenesis. Biochem Biophys Res Commun. 2014;443:495-9.
[42] DiCostanzo AC, Thompson JR, Peterson FC, Volkman BF, Ramirez-Alvarado M. Tyrosine residues mediate fibril formation in a dynamic light chain dimer interface. J Biol Chem. 2012;287:27997-8006.
[43] Nokwe CN, Hora M, Zacharias M, Yagi H, John C, Reif B, et al. The Antibody Light-Chain Linker Is Important for Domain Stability and Amyloid Formation. J Mol Biol. 2015;427:3572-86.
[44] Bodi K, Prokaeva T, Spencer B, Eberhard M, Connors LH, Seldin DC. AL-Base: a visual platform analysis tool for the study of amyloidogenic immunoglobulin light chain sequences. Amyloid : the international journal of experimental and clinical investigation : the official journal of the International Society of Amyloidosis. 2009;16:1-8.
[45] Sormanni P, Camilloni C, Fariselli P, Vendruscolo M. The s2D method: simultaneous sequence-based prediction of the statistical populations of ordered and disordered regions in proteins. J Mol Biol. 2015;427:982-96.
[46] Cilia E, Pancsa R, Tompa P, Lenaerts T, Vranken WF. From protein sequence to dynamics and disorder with DynaMine. Nature communications. 2013;4:2741.

[47] Sormanni P, Amery L, Ekizoglou S, Vendruscolo M, Popovic B. Rapid and accurate in silico solubility screening of a monoclonal antibody library. Sci Rep. 2017;7:8200.
[48] Sormanni P, Aprile FA, Vendruscolo M. The CamSol method of rational design of protein mutants with enhanced solubility. J Mol Biol. 2015;427:478-90.
[49] Wolf Perez AM, Sormanni P, Andersen JS, Sakhnini LI, Rodriguez-Leon I, Bjelke JR, et al. In vitro and in silico assessment of the developability of a designed monoclonal antibody library. mAbs. 2018.
[50] Goldenzweig A, Goldsmith M, Hill SE, Gertman O, Laurino P, Ashani Y, et al. Automated Structure- and Sequence-Based Design of Proteins for High Bacterial Expression and Stability. Molecular cell. 2016;63:337-46.
[51] Schymkowitz J, Borg J, Stricher F, Nys R, Rousseau F, Serrano L. The FoldX web server: an online force field. Nucleic acids research. 2005;33:W382-8.
[52] Broom A, Jacobi Z, Trainor K, Meiering EM. Computational tools help improve protein stability but with a solubility tradeoff. J Biol Chem. 2017;292:14349-61.
[53] Dunbar J, Fuchs A, Shi J, Deane CM. ABangle: characterising the VH-VL orientation in antibodies. Protein Eng Des Sel. 2013;26:611-20.
[54] Costantini S, Colonna G, Facchiano AM. Amino acid propensities for secondary structures are influenced by the protein structural class. Biochem Biophys Res Commun. 2006;342:441-51.
[55] Kazanov MD, Igarashi Y, Eroshkin AM, Cieplak P, Ratnikov B, Zhang Y, et al. Structural determinants of limited proteolysis. Journal of proteome research. 2011;10:3642-51.
[56] Blancas-Mejia LM, Tischer A, Thompson JR, Tai J, Wang L, Auton M, et al. Kinetic control in protein folding for light chain amyloidosis and the differential effects of somatic mutations. J Mol Biol. 2014;426:347-61.
[57] Hernandez-Santoyo A, del Pozo Yauner L, Fuentes-Silva D, Ortiz E, Rudino-Pinera E, Sanchez-Lopez R, et al. A single mutation at the sheet switch region results in conformational changes favoring lambda6 light-chain fibrillogenesis. J Mol Biol. 2010;396:280-92.
[58] Rennella E, Morgan GJ, Kelly JW, Kay LE. Role of domain interactions in the aggregation of full-length immunoglobulin light chains. Proc Natl Acad Sci U S A. 2019;116:854-63.
[59] Brumshtein B, Esswein SR, Salwinski L, Phillips ML, Ly AT, Cascio D, et al. Inhibition by small-molecule ligands of formation of amyloid fibrils of an immunoglobulin light chain variable domain. eLife. 2015;4:e10935.
[60] Morgan GJ, Yan NL, Mortenson DE, Rennella E, Blundon JM, Gwin RM, et al. Stabilization of amyloidogenic immunoglobulin light chains by small molecules. Proc Natl Acad Sci U S A. 2019;116:8360-9.
[61] Chiti F, Dobson CM. Protein Misfolding, Amyloid Formation, and Human Disease: A Summary of Progress Over the Last Decade. Annual review of biochemistry. 2017;86:27-68.
[62] Dunbar J, Deane CM. ANARCI: antigen receptor numbering and receptor classification. Bioinformatics. 2016;32:298-300.
[63] Kabsch W. Xds. Acta Crystallogr D Biol Crystallogr. 2010;66:125-32.
[64] Vagin AA, Teplyakov A. MOLREP: an automated program for molecular replacement. Journal of Applied Crystallography. 1997;30:1022-25.
[65] Emsley P, Cowtan K. Coot: model-building tools for molecular graphics. Acta Crystallogr D Biol Crystallogr. 2004;60:2126-32.

[66] Adams PD, Afonine PV, Bunkoczi G, Chen VB, Davis IW, Echols N, et al. PHENIX: a comprehensive Python-based system for macromolecular structure solution. Acta Crystallogr D Biol Crystallogr. 2010;66:213-21.
[67] Bricogne G, Blanc E, Brandl M, Flensburg C, Keller P, Paciorek W, et al. BUSTER version X.Y.Z. 2017.
[68] Chen VB, Arendall WB, 3rd, Headd JJ, Keedy DA, Immormino RM, Kapral GJ, et al. MolProbity: all-atom structure validation for macromolecular crystallography. Acta Crystallogr D Biol Crystallogr. 2010;66:12-21.
[69] Krissinel E, Henrick K. Inference of macromolecular assemblies from crystalline state. J Mol Biol. 2007;372:774-97.
[70] Piovesan D, Minervini G, Tosatto SC. The RING 2.0 web server for high quality residue interaction networks. Nucleic acids research. 2016;44:W367-74.

		Candidate mutation			Frequency in M LCs MSA			FoldX ΔΔG(kcal/mol)			
Residue number	H6 residue	M LCs Consensus	PROSS server	PROSS Ranking	H6 residue	PROSS mutation	M-consensus mutation	PROSS mutation	M-consensus mutation	interface	Solvent exposure (%)
12	A	G	G	5	6	55	orted if different from PROSS	0,72	orted if different from PROSS	0	9,2
43	R	Q	Q	4	6	29	0,13	0	64,6		
44	T	A	A	6	2	73		0,08		1	67,2
47	**V**	**L**	M	2	0	3	85	-0,97	**-1,27**	0	36
70	**T**	**N**	**N**	5	35	49		**-1,11**		0	37,5
75	**G**	**T**	**T**	1	5	64		**-1,06**		0	10,9
81	T	A	A	7	8	56		-0,18		0	62,8
82	G	E	E	6	17	59		-0,11		0	60,6

Table 1. Shortlisted and selected stabilising mutations. Candidate mutation sites for H6. H6 residues are listed in the second column; in the third are the consensus residues from the MSA of M-LC sequences; the fifth column lists the mutations suggested by the PROSS web server, which happen to be identical to the consensus amino acid with the exception of site 47. At this site, the M-consensus mutation was chosen because it was predicted to be more stabilising by FoldX, and because the V to L substitution is chemically more conservative than V to M. The table also reports the PROSS ranking of mutations corresponding to the energy threshold that selected them (1 being the most stabilising), the frequency of the H6 residues and of their candidate substitutions in the M LCs MSA, and the FoldX ΔΔG for each mutation. Mutations in bold are those selected for experimental validation.

Wavelength (Å)	1.07227
Resolution range (Å)	38.46-2.10 (2.16-2.10)
Space group	I 1 2 1
Unit cell constants (Å °)	79.89, 72.58, 84.84; 90.00, 105.67, 90.00
Unique reflections	27333 (2214)
Multiplicity	3.4 (3.3)
Completeness (%)	99.9 (99.0)
Mean I/sigma(I)	13 (0.8)
Wilson B-factor ($Å^2$)	53.5
R-merge[a]	0.04 (1.211)
CC1/2	0.999 (0.58)
Refinement	
R-work[b]	0.206
R-free[b]	0.238
Average B-factor ($Å^2$)	68
Number of non-hydrogen atoms	3341
Protein	3185
Solvent	126
RMS (bonds, Å)	0.010
RMS (angles, °)	1.19
Ramachandran plot (%)	
Most favoured	98
Allowed	2
Rotamer outliers (%)	2

Table 2: Data collection and refinement statistics for mH6 crystal structure.

[a] $R_{merge} = \Sigma_{hkl} \Sigma_j |I_{hkl,j} - \langle I_{hkl} \rangle| / \Sigma_{hkl} \Sigma_j I_{hkl,j}$, where I_{hkl} is the observed intensity and $\langle I_{hkl} \rangle$ is the average intensity for the hkl reflection.

[b] $R_{work} = \Sigma_{hkl} |F_o - F_c| / \Sigma_{hkl} F_o$ for all data except 5%, which were used for the R_{free} calculation.

Values given in parenthesis refer to the high-resolution shell.

Figure 1

Click here to access/download;Figure;Fig_1_def.jpg

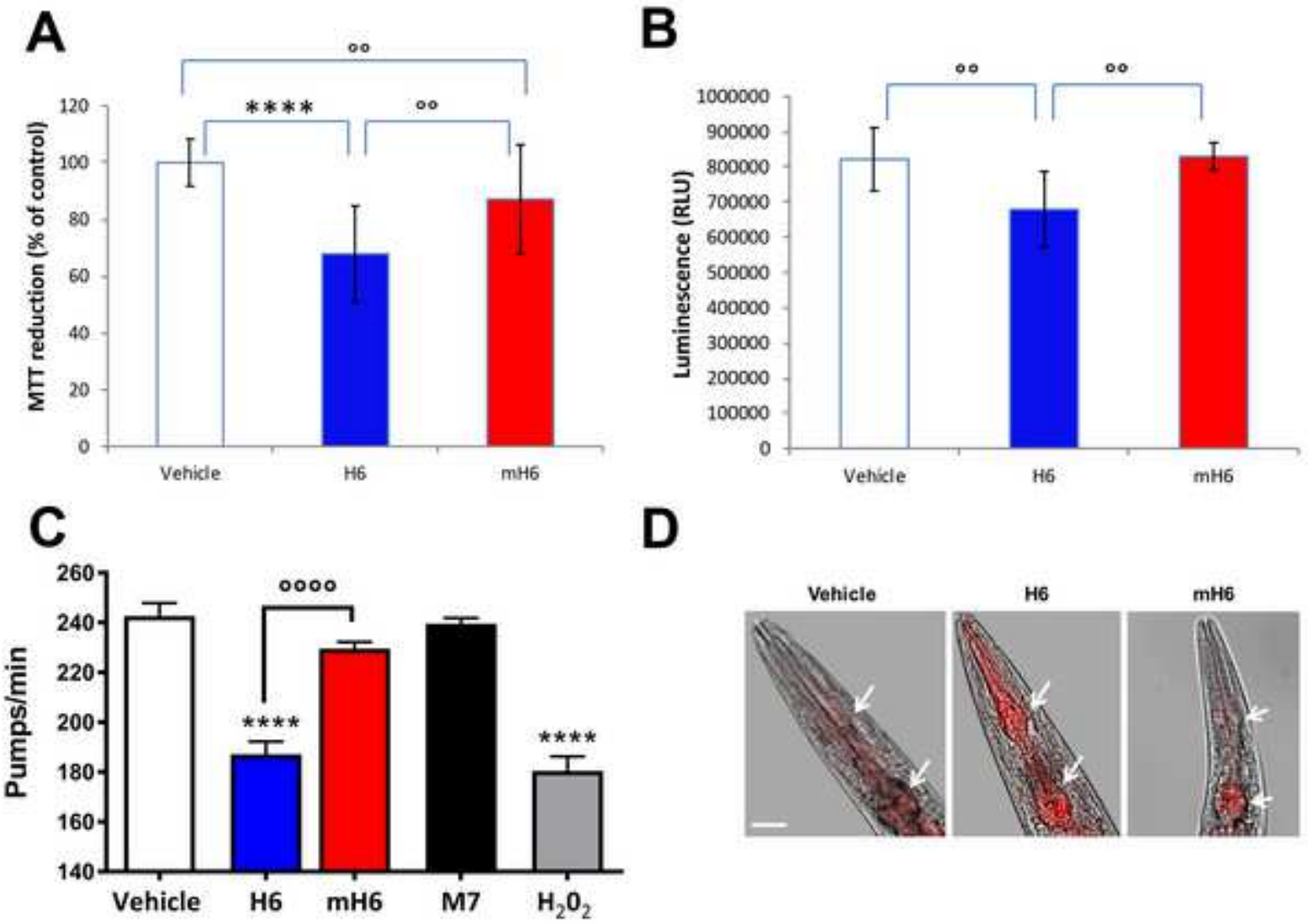

Figure 3

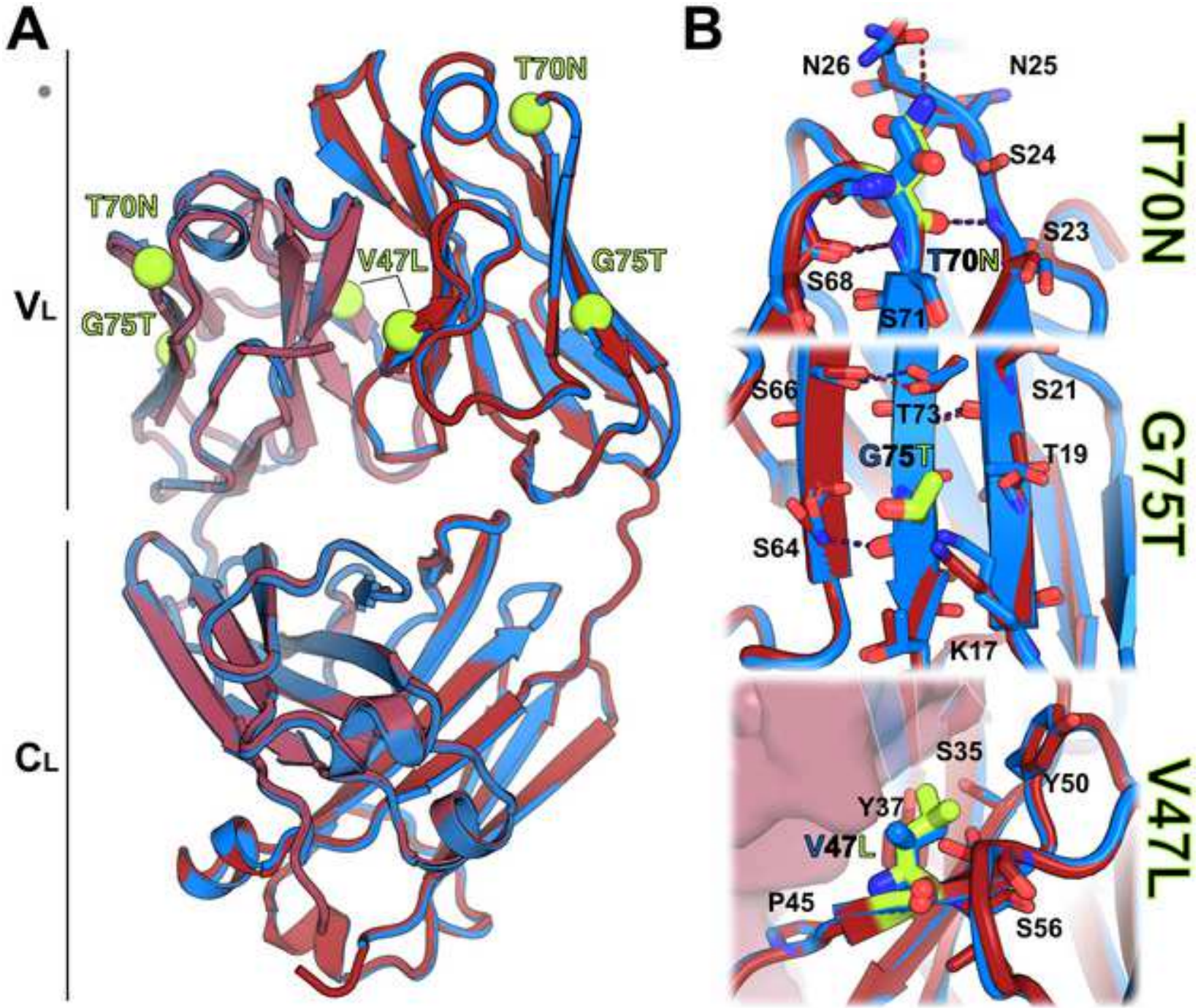

Figure 4

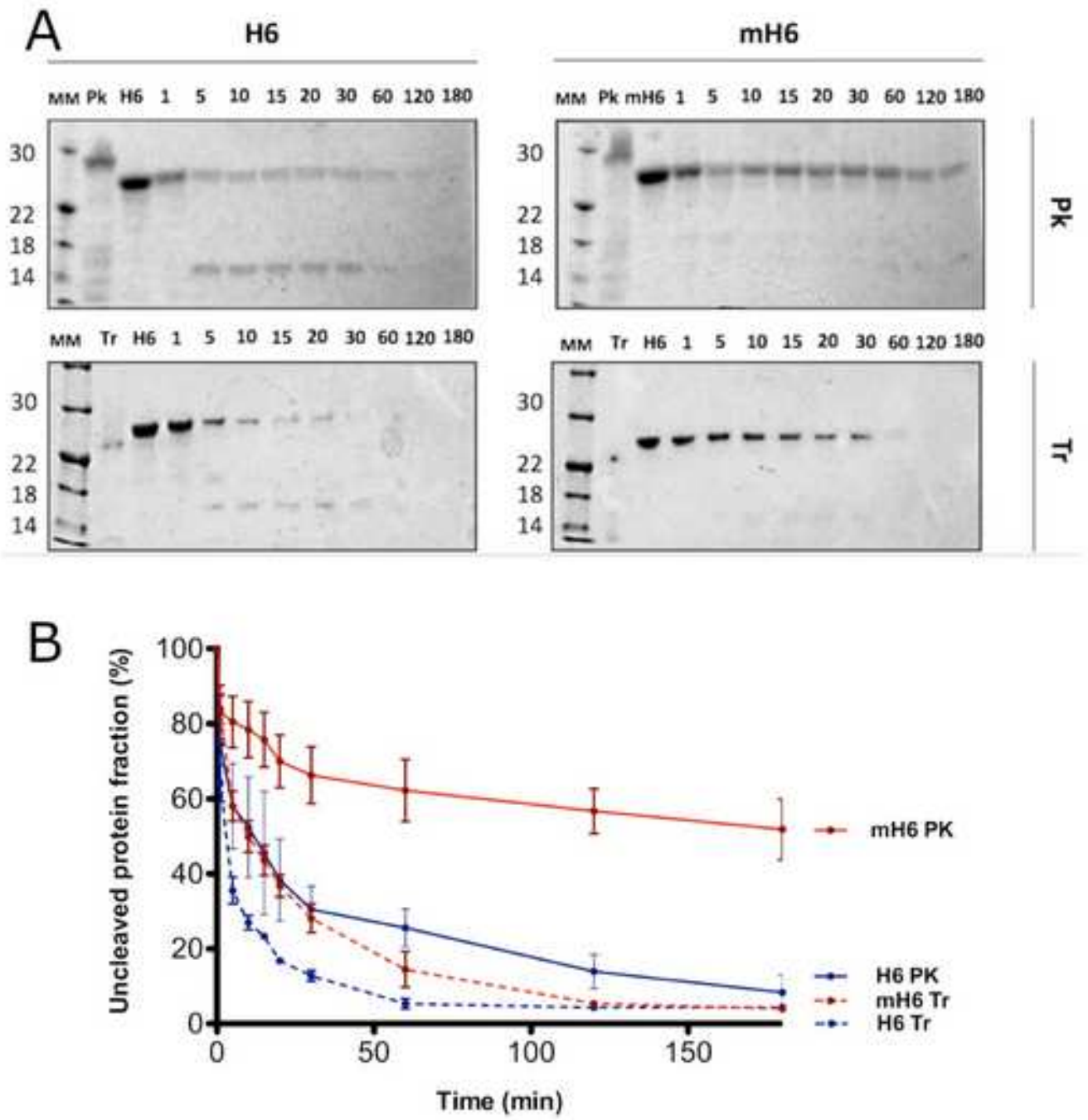

Figure 5

Click here to access/download;Figure;Fig_5_rev.jpg

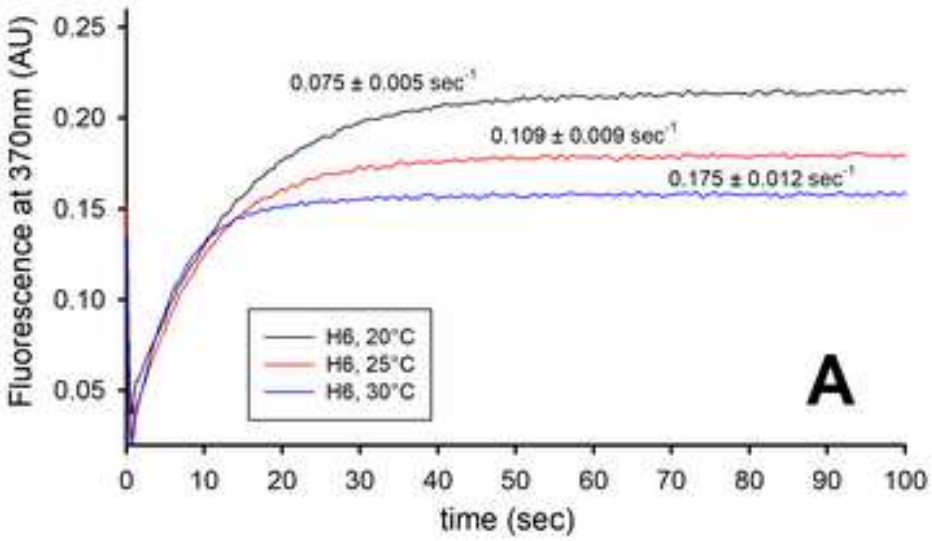

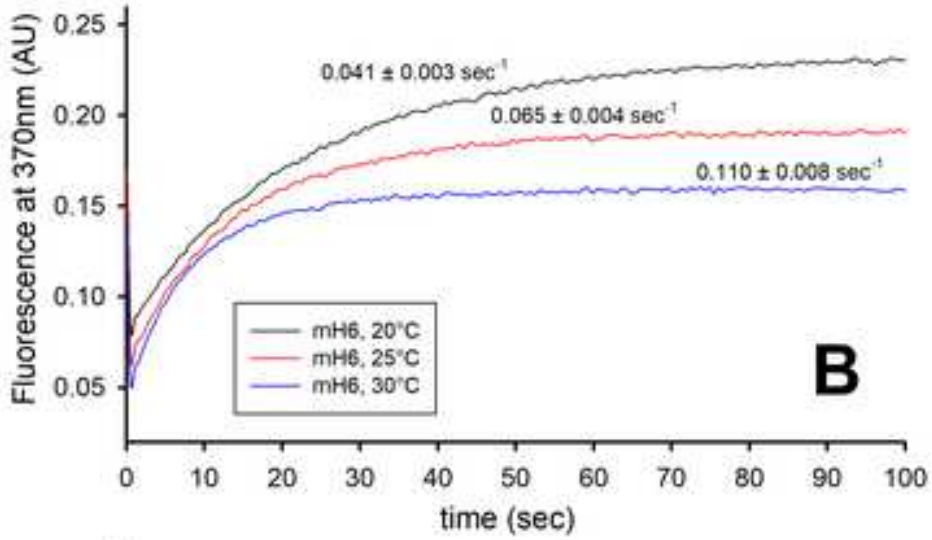

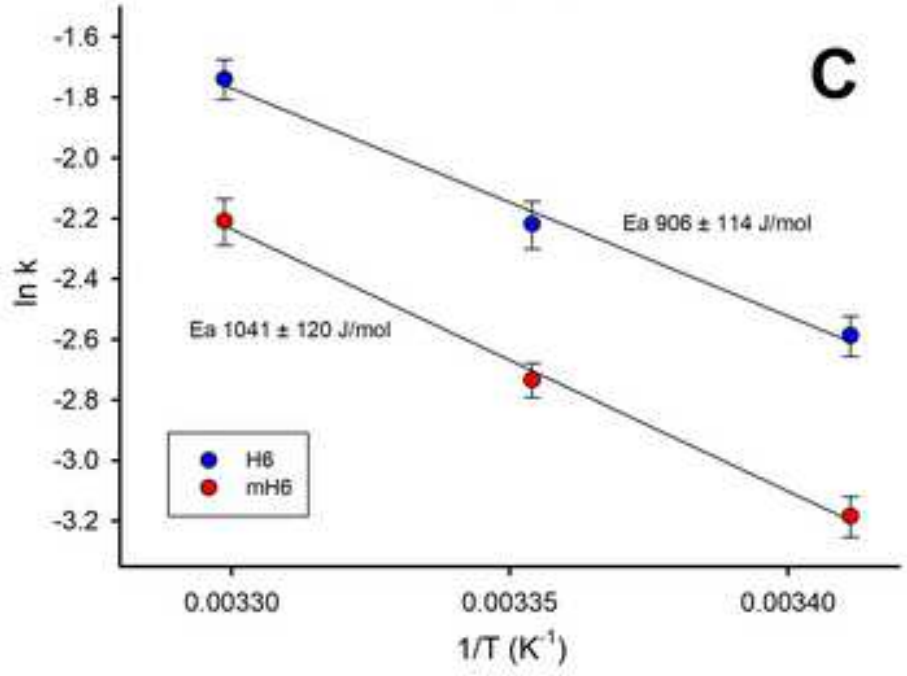

Figure 2 revised